Investigation on Placement of Battery Energy Storage System in Wave Power Conversion System

Renqi Guo, Yueqi Wu, Xiandong Ma, George Aggidis, and Nan Zhao, *Member, IEEE*

***Abstract*—Wave Energy Converter (WEC) systems harness kinetic energy from ocean waves, with the power take-off (PTO) system facilitating the conversion to electrical power. To integrate the WEC system into the AC grid, a voltage-sourced converter (VSC) with grid forming (GFM) control becomes essential, especially in future grids with high penetration of renewables. A battery energy storage system (BESS) is typically coupled with the WEC system to enhance integration. BESS can be connected either on the DC side or the AC side, leading to different topologies and performance outcomes. When placed on the DC side (WECd) and controlled by GFM, the overall system can accurately track the reference power and provide grid support. However, if a GFM-controlled BESS is on the AC side (WECa), although the grid-side VSC requires reduced capacity, it may experience delays in aligning with the WEC power as compared to its reference power curve due to DC voltage variations, potentially leading to grid power imbalances. This paper presents the integration of a linear generator (LG)-based multi-axis WEC system into the AC grid, with a detailed comparison regarding the placement of BESS. A novel GFM control strategy is proposed to improve the reference power tracking accuracy of WECa system. Additionally, parameter design is explored through transfer function analysis. The results from simulation show that the proposed control effectively improves the system power tracking ability and controllability of WECa system, achieving performance comparable to WECd system. Meanwhile, WECa requires less capacity for the batteries.**

***Index Terms*—wave energy converter, grid-forming converter, battery energy storage system, grid integration**

I. Introduction

As climate concerns become serious, renewable energy has been a popular topic during the past decades. Renewable energy can be converted into electricity through various topologies, significantly reducing carbon emissions when compared with traditional generator-based power plants. European countries stand to benefit significantly from the utilization of renewable energy sources to achieve the target of net-zero carbon by 2030 [1]. For coastal countries, wave energy plays an important role in their renewable plans. To harness the kinetic energy of the wave and transfer it into electricity, wave energy converter (WEC) has been investigated for many years. Many literatures have focused on single-direction WEC, while the wave motion has more than six degrees of freedom [2]. Therefore, WECs with multiple axes can potentially absorb more power than that with a single axis. Technologically Advanced Learning Ocean System (TALOS) was proposed by researchers at Lancaster University [3] and was further developed recently [4], which is a point-absorber type WEC and has six axes Power Take-Off (PTO) system. The prototype and experimental test of TALOS in a wave tank are illustrated in Fig. 1. Fig. 2 further introduces the details design of TALOS and the wave forces in six motions. As can be seen, the hull connects the heavy ball with springs, and it generates forces after being released in the wave tank by harnessing the kinetic energy from the wave. If a hydraulic system is used as PTO, the relative motion between the ball and hull can produce force to pump the hydraulic cylinders, generating fluid that drives the hydraulic motor to generate electricity. However, hydraulic systems pose environmental risks due to potential fluid leaks [5] and involve complex dual-stage energy conversions—from mechanical to hydraulic, and back to mechanical energy to drive a generator [6]. In contrast, PTO systems with permanent magnet linear generators (PMLGs) involve only one energy conversion stage, directly transforming mechanical energy into electricity. The direct conversion results in reduced maintenance needs and high efficiency [7]. This paper focuses on a six-PMLG based power conversion system for TALOS.

Back-to-back voltage source converters (VSCs) are commonly used in renewable integration, which can decouple the fluctuated renewable resource from the stable AC grid [8]. Since the grid code requires renewable farms to participate in frequency response [9], the grid-forming (GFM) capability of future renewable power plants is increasingly important. Authors in [10] investigated the control of back-to-back VSC in the WEC system, but the priority was to increase the efficiency of the PTO system to maximize the power output. In [11], while also utilising a back-to-back structure, the focus on the WEC floater related system, the estimator and PTO control, without delving into the grid integration of WEC.

To smooth the output power and realise an enhanced grid integration, the battery energy storage system (BESS) in [12] and supercapacitor in [13] were placed on the DC link of the GFL-based WEC (here referred to WECd) system in their schemes; however, they are not designed for grid support due to the constraints of the control of VSC. Similarly, authors in [14] proposed a hybrid energy storage system with BESS and SC at DC link for output power smoothing. Researchers in [15] proposed a multi-mode control for the converter, to actively switch modes (grid feeding, grid support and grid forming)

The name of the corresponding author is Nan Zhao.

Renqi Guo, Yueqi Wu, Xiandong Ma, George Aggidis and Nan Zhao are with the School of Engineering, Lancaster University, Lancaster, UK.

(e-mails: r.guo2@lancaster.ac.uk, y.wu31@lancaster.ac.uk, xiandong.ma@lancaster.ac.uk, g.aggidis@lancaster.ac.uk, nan.zhao@lancaster.ac.uk).

according to the grid conditions. However, they considered their DC voltage to be constant with the regulation from supercapacitor and batteries and neglected the difficulties in upgrading the existing WEC system. If the existing WEC system was built without the consideration of the potential extra power from a BESS, the grid-side VSC may need to be replaced by a larger-capacity converter. Therefore, the location of BESS on the AC side (here referred to WECa) can keep the existing system unchanged and fulfil the same function of grid support. There are also many literatures discussing the mechanical storage system to help the power smoothing. Authors in [16] analysed the impact of mechanical storage at WEC generator performance, and researchers in [17] discovers the integration of WEC with flywheel to emulate inertia and smooth power. Some literature developed the GFM-based WEC system to support the grid actively. In [18], a droop controller was applied to help the grid realise the capability of frequency response. The AC-side BESS plays a significant role in the hybrid system as well [19]. Although the hybrid system in this paper included wave energy as renewables, the authors focused more on energy management schemes and did not consider detailed transients of the WEC system. In short, both WECa and WECd can actively support the grid with GFM control. The difference between the two systems is the flexibility in designing the capacity of the systems. In addition, the DC link voltage of WECd system tends to be more easily regulated than WECa system.

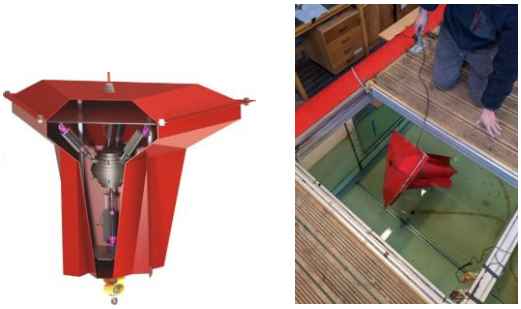

(a) (b)

Fig. 1. Prototype of TALOS [3]. (a) designed prototype; (b) experimental test in wave tank

Many literatures explore the integration of the WEC system with BESS, but few of them discuss the placement of BESS. In addition, most research assumes the DC link voltage of the WEC system remains constant, regulated by additional DC/DC converters or energy storage systems. This allows the GFL-controlled VSC to operate under maximum power point tracking (MPPT) mode or to track the forecasting power curve accurately, which may not reflect real-world scenarios. Accurate power conversion is crucial for maintaining power balance, especially in urban microgrids [20], as grid operators rely on forecasted or calculated MPPT power from renewable farms to keep the frequency stable. However, if BESS is not on the DC side and passive rectifiers are used at the interface between the WEC and the DC link, there might be a delay in the power conversion between power from the machine side and the actual power injected into the grid.

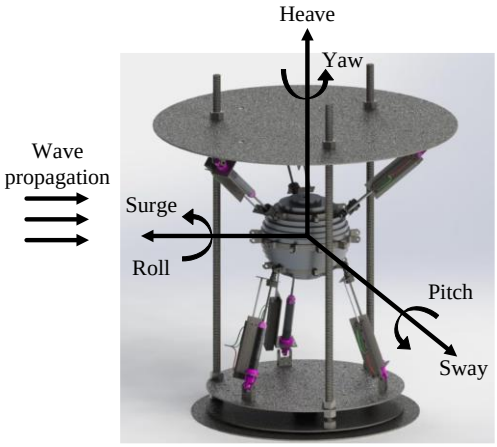

Fig. 2. Six motions of TALOS [3]

This paper investigates the two configurations of the WEC system with BESSs on the DC side and AC side, providing a detailed comparison. The primary contribution of this study is to propose a modified GFM control, which enhances the power tracking accuracy of the WECa system to be comparable to WECd system. Analysis of the detailed transfer functions shows the potential equivalence between the WECa and WECd systems can be achieved with proper parameter tuning. After tuning the parameters of the proposed control, simulations are performed for verification. Results show that the WECa system, equipped with a BESS under the modified GFM control, can fully and accurately track the reference power (forcasting or MPPT power curve). Additionally, this modified control significantly reduces the peak power requirements of the BESS compared to the WECd system.

II. Power Conversion System Modelling

A. WECd System

The WECd system is shown in Fig. 3, and it primarily comprises of six PMLGs, a BESS and a grid-side VSC. The BESS is on its DC link. TALOS absorbs the kinetic energy, which drives the PMLGs to generate electrical power. The six PMLGs are connected to the DC link via passive rectifiers, and there is a DC/DC converter between the battery and the DC link. The function of BESS is to provide/absorb the required power for smoothing power output and frequency response. Moreover, it can also stabilise the DC link voltage by controlling the DC/DC converter. The grid-side converter is a GFM-controlled VSC, which injects the required power into the grid while supporting the power system with its grid-forming capabilities. From the grid side, the GFM controlled VSC can be regarded as a voltage source, and this allows the system to actively provide frequency and voltage support.

1)PMLG and WEC

The TALOS has six dampers, and normally the six motions are considered, namely yaw, heave, pitch, sway, roll and surge. This is illustrated in Fig. 2. In our study, six PMLGs are used to capture the forces generated by the dampers.

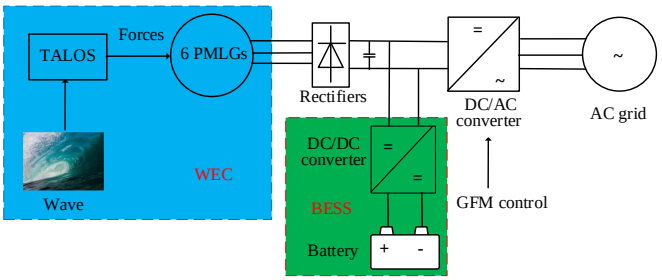

Fig. 3. WEC system with BESS at DC link [4]

Through the experiment, TALOS has two symmetries for the *x* and *y* axes, which means the force from the motions of pitch and roll are the same, and those from sway and surge are the same as well [3].

The main difference between linear generators and traditional synchronous generators is the motion of the rotor. The PMSG has a rotational rotor with constant speed, while the PMLG's rotor, named translator is not rotational and has a continuously changing speed [21]. The force from TALOS drives the translator of PMLG to generate electricity.

2)Grid-forming Control of Grid-side VSC

Different from GFL controlled VSC, the system with GFM can form the grid and be regarded as a voltage source from the perspective of the grid. In this paper, one of the most popular GFM topologies is implemented, named virtual synchronous generator (VSG) [22]. The topology of the DC/AC converter is a two-level voltage-sourced converter, with six IGBT-Diode implemented. The key of a traditional VSG is the swing equation (1), which mimics the behaviour of a traditional synchronous generator (SG). The voltage angle is determined by (1) and (2), while the voltage magnitude is controlled by reactive power which is shown in (3) [23].

$$J\frac{d\Delta\omega_{vsg}}{dt} = P_{ref} - P_e - K_d * \Delta\omega_{vsg} \quad (1)$$

$$\omega_{vsg} = \Delta\omega_{vsg} + \omega_{ref} \quad (2)$$

$$E = V_{ref} - K_q * (Q_{ref} - Q_e) \quad (3)$$

where J is the virtual inertia of VSG; K_d is the damping factor; P_{ref} and P_e are reference active power and output active power respectively; $\Delta\omega_{vsg}$ represents the frequency change of VSG ;ω_{vsg} and ω_{ref} are the frequency of VSG and reference value; E, V_{ref}, K_q, Q_{ref} and Q_e are the virtual electric potential, reference voltage for the converter, reactive power gain, reference reactive power and output reactive power of VSG.

Note that the active power reference for VSG has two choices depending on the requirement of the grid. The MPPT in the paper used a simplified version of constant voltage mode. With the fixed reference voltage, the P_{ref} will be the measured direct power output of PMLG P_{lg} with the neglection of wave profiles. If the WEC system operates at maximum power point tracking (MPPT) mode, the P_{ref} will be the direct power output of PMLG P_{lg}. When the grid requires the WEC system to operate at constant power, then the P_{ref} is set to be constant and BESS can compensate for the power difference between P_{lg} and P_{ref}.

The virtual impedance aims at generating reference voltage to the voltage controller for the converter. It also provides a link between VSG and the grid. X_v is the virtual impedance of VSG and r_v is virtual resistance. u_o and i are the output voltage and current of VSG respectively. This relationship is expressed in (4).

$$u_o = E - i*(r_v + jX_v) \quad (4)$$

VSG control contains an outer voltage controller, an inner current controller and pulse-width modulation (PWM), which controls the dynamics of the converter. The voltage controller is introduced by (5) and (6), and the current controller is not included in this part due to its same structure as the voltage controller.

$$i^*_{dvsc} = K_{pv}(u^*_{od} - u_{od}) + K_{iv}\int(u^*_{od} - u_{od}) - \omega_{vsg}c_f u_{oq} \quad (5)$$

$$i^*_{qvsc} = K_{pv}(u^*_{oq} - u_{oq}) + K_{iv}\int(u^*_{oq} - u_{oq}) + \omega_{vsg}c_f u_{od} \quad (6)$$

where i^*_{dvsc} and i^*_{qvsc} are the reference current for the current controller, which is produced by the voltage controller; K_{pv} and K_{iv} are the PI gains of the voltage controller; c_f is the filter capacitance of VSG.

The power output equations in the DQ-frame are (7) and (8). The output power P_e and Q_e are also respectively the feedback values used in active power control (1) and reactive power control (3) at the same time.

$$P_e = \frac{3}{2}(u_{od}i_d + u_{oq}i_q) \quad (7)$$

$$Q_e = \frac{3}{2}(-u_{od}i_q + u_{oq}i_d) \quad (8)$$

3)Control of DC/DC Converter

The topology of DC/DC converter is a bidirectional dc-dc converter, consisting of two IGBTs. The function of the BESS is to compensate for the instantaneous power difference between the desired power injected into the AC grid and the direct power output from PMLGs, i.e. smoothing the power output for stable operation of the grid. It can also provide additional power for frequency response. Since the PWM generation requires the participation of DC link voltage, a stable DC voltage is beneficial for the quality of VSC output. Therefore, the second target of the battery is to stabilize the DC link voltage. The control diagram of the DC/DC converter is shown in Fig. 4, which is PI control that regulates the DC voltage with the reference voltage.

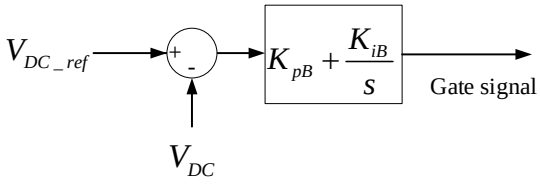

Fig.4. Control of DC/DC converter

The WECd system behaves like a synchronous generator which can actively support the grid in frequency and voltage,

and it can track its reference power with a controllable inertia effect through the swing equation (1).

B. WECa System

In the WECa system, the BESS is connected to the AC grid rather than the DC link of the WEC system. Since the passive rectifiers are implemented for simplicity and cost savings, the DC link voltage of the WEC system needs to be regulated by the WECd converter. Therefore, the grid-side VSC adopts a classical GFL control, which regulates the DC voltage [24, 25] and the reactive power control (or grid voltage support). The battery with VSG control provides the frequency response and voltage support for the AC grid. The detailed schemes are presented in Fig. 5 and the expressions of GFL control are as (9) and (10).

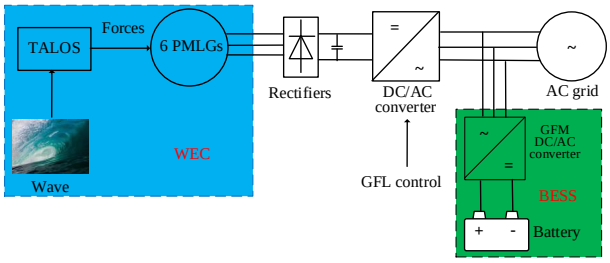

Fig.5. WEC with BESS at AC side

$$i_{dref} = K_{p1}(V_{dcr} - V_{dc}) + K_{i1}\int (V_{dcr} - V_{dc}) \tag{9}$$

$$i_{qref} = -\frac{2}{3V_{sd}}(Q_{ref} - Q_{gfl}) \tag{10}$$

where i_{dref} and i_{qref} are the reference current for the VSC in the d-axis and q-axis, V_{dcr} is the reference DC link voltage, V_{dc} is the measured DC link voltage, V_{sd} is the voltage measured by the phase lock loop (PLL) is d-axis, Q_{ref} is the reference reactive power, Q_{gfl} is the reactive power injected into the AC grid, K_{p1} and K_{i1} are the PI gains.

Similar to the swing equation (1), the VSG-controlled BESS can support the grid frequency with inertia and damping effects, and DC link capacitance also provides an uncontrolled inertia effect through the voltage dynamics as (11).

$$P_{lg} - P_{gfl} = C_d V_{dc} \frac{dV_{dc}}{dt} \tag{11}$$

where P_{lg} is the sum of six PMLGs' power, P_{gfl} is the power from GFL controlled converter, C_d is the DC link capacitance.

From (11), there is always a difference between the output power of PMLGs and the output from VSC, which leads to an inertia effect; however, this cannot be straightforward controlled like VSG. Based on (1), K_d and J are all controllable to adjust the output power, but for (11), the capacitor is fixed. Therefore, the flexibility of control is limited, and the power difference causes a delay effect. This may result in unwanted performance such as power imbalance. To understand the difference between WECa and WECd systems, a step power from the DC link arises at 2s and Fig. 6 shows the power outputs and DC voltage variations under a power step from DC link of WEC (equivalent to PMLG's power step).

In the Fig. 6, P_b is the power from BESS, P_d is the measured power on DC link of WEC, and P_{grid} is the total power injected

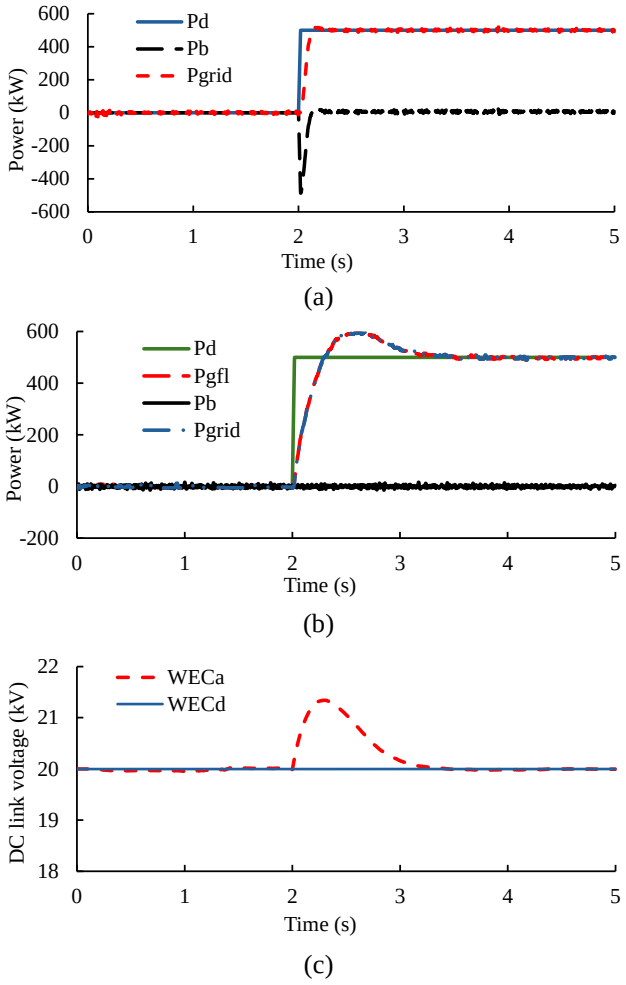

Fig.6. Power step response from DC link of WEC system. (a) WECd system, (b) WECa system, (c) DC link voltage of two WEC systems

into the AC grid. Detailed parameters will be given afterwards. The DC link variation leads to a noticeable delay in the WECa system when compared with the WECd system. It takes approximately 1s for the GFL to fully follow the step power.

C. Modified VSG Control

To reduce the delay of WECa system to a desired value and track WEC's MPPT power with desired inertia, a modification is implemented into the traditional VSG control. This is shown in Fig. 7. From the diagram, K_{p2} and K_{i2} are the PI gains of the modification loop, θ_{vsg} is the overall angle of modified VSG, $P_{in} = P_{lg} - P_{gfl}$ is the input of the modified loop and *H(s)* describes the transfer function from θ_{vsg} to P_e. Detailed expression of *H(s)* can be found in [26], and its simplified form H_0 is expressed as (12).

$$H_0 = \frac{3}{2}\frac{E_0 a}{(R^2 + X^2)^2} \tag{12}$$

where $a = V_{g0}(R^2+X^2)(R\sin\delta_0 + X\cos\delta_0) - 2V_{g0}r_v R^2 \sin\delta_0 + 2E_0 r_v X \sin\delta_0 (R\sin\delta_0 - X\cos\delta_0)$ and E_0, V_{g0} and δ_0 are all initial

operating points. In this paper, δ_0 is 0 for simplification. R is the sum of VSG's virtual resistance and grid resistance, X is the sum of VSG's virtual impedance and grid impedance.

The proposed modified VSC control contains a low-pass filter (LPF) and a PI controller. The VSG can participate in compensating and adjusting the performance of GFL while maintaining its original features. The LPF is for filtering the measured signal. If the LPF is combined with the PI controller in the transfer function, it can introduce a pole at $-\omega_l$. However, this pole is far from the origin, normally it is regarded as a non-dominant pole that can be neglected. (13) is the simplified transfer function of the modified control.

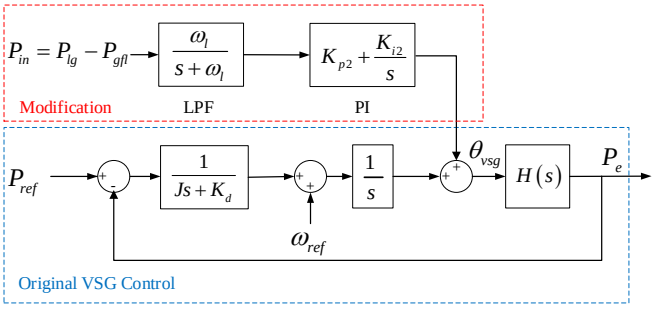

Fig.7. Modified VSG control

$$\frac{P_e}{P_{in}} = H_0(K_{p2} + \frac{K_{i2}}{s}) \tag{13}$$

The modified control in (13) has a corner frequency as $\frac{K_{i2}}{K_{p2}}$ and a crossover frequency as $\sqrt{\frac{K_{i2}^2 H_0^2}{1-K_{p2}^2 H_0^2}}$. To ensure a stable operation, both frequencies should be below the grid frequency, and the corner frequency should be larger than cross over frequency [27]. The relationship is shown as (14). This guarantees an adequate phase margin and avoids instability.

$$\sqrt{\frac{K_{i2}^2 H_0^2}{1-K_{p2}^2 H_0^2}} < \frac{K_{i2}}{K_{p2}} < \omega_g \tag{14}$$

In this paper, K_{i2} and K_{p2} are initially selected as 9e-6 and 1.5e-7. This yields a corner frequency of 60 rad/s and a crossover frequency of 25.3 rad/s. Further discussion will be given in the next section.

III. Transfer Function Development and Analysis

In this section, a step power is used as the input of the transfer functions for both GFL and modified VSG control.

A. GFL control

Recall (11), linearizing around the operation point V_0 for small signal analysis, one can get (15).

$$\Delta V_{dc}(s) = \frac{\Delta P_{lg} - \Delta P_{gfl}}{C_d V_0 s} \tag{15}$$

The PI controller of GFL control (9) can be rewritten in the form of small signal as well. Assuming P_{gfl} can be calculated with the reference d-axis current as (16), substituting the expression of the d-axis current from the PI controller into (16), the P_{gfl} can be represented by (17).

$$\Delta P_{gfl}(s) = \frac{3}{2} V_g \Delta I_d(s) \tag{16}$$

$$\frac{\Delta P_{gfl}}{\Delta V_{dc}} = \frac{3}{2} V_g (K_{p1} + \frac{K_{i1}}{s}) \tag{17}$$

Substitute (15) into (17) and rearrange the equations, the closed-loop transfer function from ΔP_{lg} to ΔP_{gfl} is expressed as (18).

$$G_1(s) = \frac{3V_g K_{p1} s + 3V_g K_{i1}}{2C_d V_0 s^2 + 3V_g K_{p1} s + 3V_g K_{i1}} \tag{18}$$

B. Modified VSG Control

The open-loop transfer function of the modified part is as (19), and that of the original VSG's is presented in (20).

$$\theta_1(s) = (K_{p2} + \frac{K_{i2}}{s})\Delta P_{in} \tag{19}$$

$$\theta_2(s) = P_e(s) \cdot \frac{1}{Js + K_d} \cdot \frac{1}{s} \tag{20}$$

Since H_0 describes the relationship between $P_e(s)$ and $(\theta_1 + \theta_2)$, the closed-loop transfer function (21) combines (19) and (20) with the consideration of feedback of the swing equation.

$$P_e(s)(1 + H_0 \frac{1}{Js^2 + K_d s}) = H_0(K_{p2} + \frac{K_{i2}}{s})P_{in}(s) \tag{21}$$

Note that P_{in} is actually equal to $P_{lg} - P_{gfl}$, rearranging (21) and solving for $P_e(s)$, the full closed-loop transfer function from P_{lg} to P_e is represented by (22).

$$G_2(s) = \frac{H_0(K_{p2}s + K_{i2})(Js + K_d)(1 - G_1(s))}{Js^2 + K_d s + H_0} \tag{22}$$

Considering the parallel operation of the WEC and BESS, the total transfer function $G_3(s)$ from P_{lg} to the overall grid power P_{grid} is the sum of $G_1(s)$ and $G_2(s)$.

$$G_3(s) = \frac{P_{grid}}{P_{lg}} = G_1(s) + G_2(s) \tag{23}$$

C. Model Verification

Given the initial parameters in Table I, a step power from 0 to 500kW occurs at 2s. Responses from both electromagnetic transient (EMT) model and transfer functions are compared for

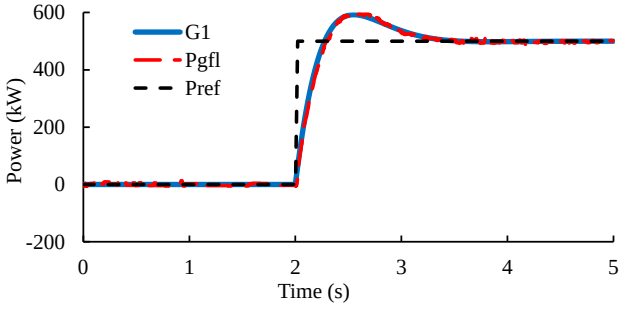

(a)

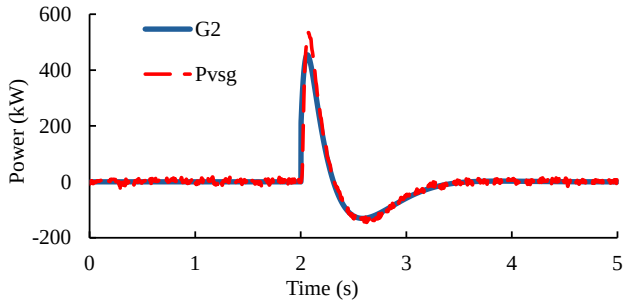

(b)

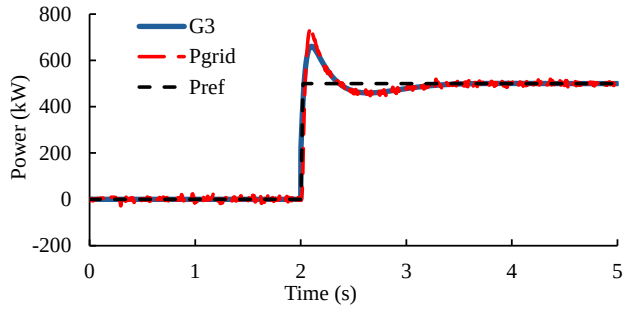

(c)

Fig.8. Response of 500kW step power. (a) GFL and $G_1(s)$, (b) VSG and $G_2(s)$, (c) Overall output and $G_3(s)$.

verification of the accuracy of transfer functions, which is shown in Fig. 8. The responses of transfer functions coincide with the corresponding model outputs, which illustrates the accuracy of the transfer functions.

Regarding the responses, the GFL itself has a delay effect that cannot track accurately, while modified VSG can help this and achieve a fast-tracking response. However, there is a noticeable surge, which will be discussed in the following section for parameter analysis.

D. Parameter Design

The stability of a transfer function is that all poles have negative real parts. Recall $G_1(s)$ and $G_2(s)$, the two transfer functions have their poles placed at the left-half plane since all coefficients of the denominators are positive. Therefore, the sum of $G_1(s)$ and $G_2(s)$ should have all poles at the left-half plane as well.

TABLE I. INITIAL SYSTEM SETTINGS

Symbol	Name	Value
S_n	System nominal apparent power	2 MVA
V_{base}	Base line voltage	10 kV
V_{g0}, E_0	RMS voltage of initial grid and VSG	8165 V
r_f	Filter resistance	0.1 pu
l_f	Filter inductance	0.5 pu
C_f	Filter capacitance	42 μF
C_d	DC link capacitance	0.002 F
ω_{ref}	Reference frequency	314.159 rad/s
J	Inertia	2600 Kg ∗ m^2
K_d	Droop/damping gain	1.59e5
K_q	Reactive power droop	0.01
ω_l	cutoff frequency of LPF	30 rad/s
r_v	Virtual resistance	0.4 pu
l_v	Virtual inductance	0.25 pu
r_g	line resistance	0.2 pu
l_g	Line inductance	0.8 pu
K_{p1}/K_{i2}	PI controller of GFL	0.02/0.05
K_{p2}/K_{i2}	PI controller of modified VSG	1.5e-7/90e-7
K_{pc}/K_{ic}	GFM Current controller P/I	0.161/19.54
K_{pv}/K_{iv}	GFM voltage controller P/I	9.244/1327
t_s	Sampling time	$1.481e(-5)$s
φ_{PM}	Flux of PMLG	40Wb
γ	Polar pitch	0.1m
R_s	Stator resistance	0.26 Ohm
L_s	Stator inductance	30 mH

From Fig. 9, the bode plot of $G_1(s)$, a small K_{p1} leads to a small phase margin and a resonance at low frequency range, while K_{i1} has a neglectable impact on these characteristics. Since this paper focuses more on the modified VSG control, K_{p1} and K_{i1} are kept at the initial value. Note that all the initial parameters in Table I are regarded as 1 pu.

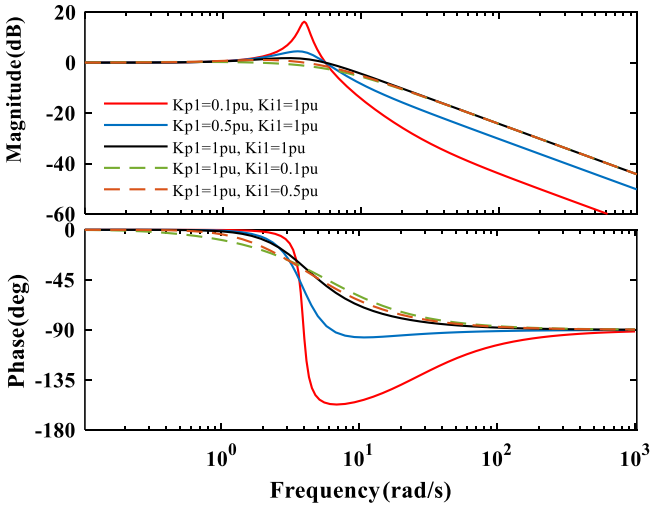

Fig. 9. Frequency characteristics of $G_1(s)$

To study the dynamics of modified VSG control, the transfer function (24) from P_{in} to P_e can be investigated, which means the change of P_{gfl} is neglected during a very short time period.

$$G_4(s) = \frac{H_0(K_{p2}s + K_{i2})(Js + K_d)}{Js^2 + K_d s + H_0} \tag{24}$$

This transfer function has the same poles as a traditional VSG control (25) without consideration of its reactive power control. This indicates that the adding feedforward loop does not influence the original VSG's stability criterion, damping ratio and natural frequency.

$$G_5(s) = \frac{\Delta P_e}{\Delta P_{ref}} = \frac{H_0}{Js^2 + K_d s + H_0} \tag{25}$$

The equivalent inertia of this modified VSG remains the same as a traditional one. To investigate the parameter's impacts on (24), J, K_d and H_0 must satisfy the stability requirement of (25) first, because the VSG needs to maintain its original function, such as frequency response and ability to follow its reference power.K_d should be designed according to the requirement of frequency support. In this paper, assuming VSG can provide 1MW with 1Hz change of grid frequency, K_d here can be calculated as $1e6/2\pi = 1.59e5$. Keeping K_d fixed at 1 pu, J and H_0 can highly influence the damping ratio $K_d/2\sqrt{JH_0}$ and natural frequency $\sqrt{H_0/J}$ of the system.

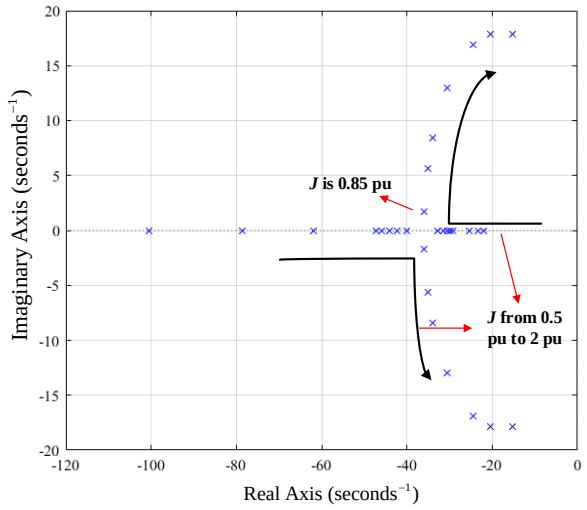

(a)

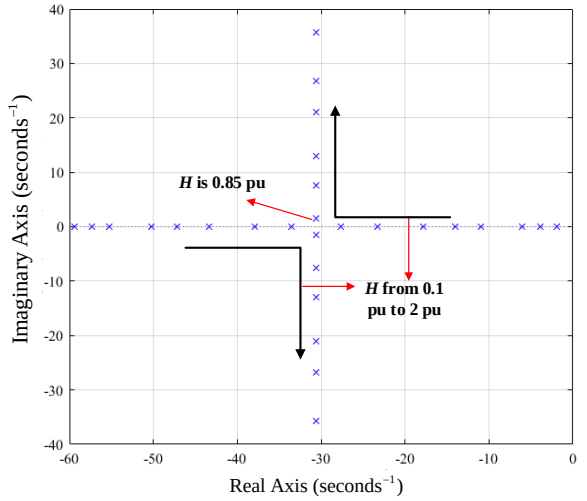

(b)

Fig. 10. Poles of $G_5(s)$. (a) Different J, (2) Different H_0.

Fig. 10 shows the pole plot of $G_5(s)$. It illustrates that when J or H_0 is below approximately 1 pu, the poles are on the real axis with a damping ratio greater than 1, which means the system is in overdamping situation. Although this could reduce the oscillation or overshoot of the system, it might bring a relatively slow response time. In this model, considering the detailed analysis of overshoot and response time in [28], J and H_0 are selected from 0.8-1.2 pu.

Recall $G_4(s)$, the change of poles is the same as $G_5(s)$, so the pole distribution in Fig.10 can be applied for (24) as well. The expansion of the numerator of (24) is $H_0K_{p2}Js^2 + (H_0K_{i2}J + H_0K_{p2}K_d)s + H_0K_{i2}K_d$.The initial and steady state values of (24) can be estimated as (26) and (27) respectively.

$$\lim_{t\to 0^+} G_4(t) = \lim_{s\to\infty} G_4(s) \approx \frac{H_0K_{p2}Js^2}{Js^2} = H_0K_{p2} \tag{26}$$

$$\lim_{t\to\infty} G_4(t) = \lim_{s\to 0} G_4(s) \approx K_{i2}K_d \tag{27}$$

This reflects the instant power that VSG can provide at the beginning of a transient. Based on different delays in the system, K_{p2} can be altered. In addition, K_{i2} can be flexibly adjusted to get a desired power output. Fig. 11 shows the plot of the zeros. Normally, when the zero is closer to the conjugate poles, the oscillation of the system will be reduced. Therefore, considering the overshoot, oscillation and the relationship deduced in (14), the K_{p2} remains at 1pu, while K_{i2} is adjusted to 0.5pu (the PI gain is then 1.5e-7/45e-7).

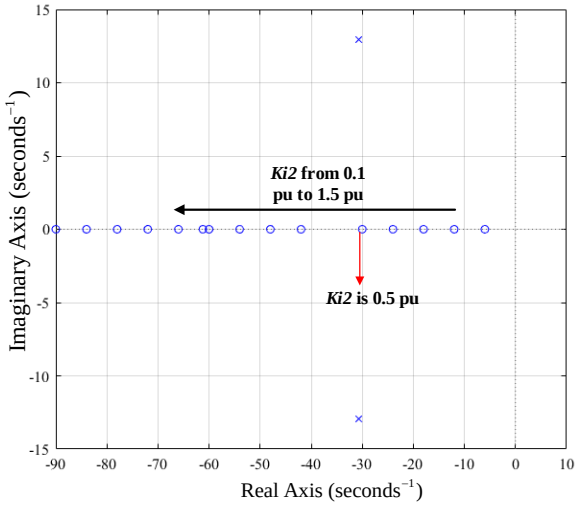

Fig. 11. Zeros maps of $G_4(s)$

The same step response is tested for WECd system under different selection of K_{i2}, which is shown in Fig. 12. It can be seen that K_{i2} has significant impacts on the system response. Fig. 12 (b) shows the power output of different parts. In Fig. 13, WECa1 represents original WECa, while WECa2 is the modified WECa. It shows that the modified WECa system can achieve a similar performance as the WECd system. Compared with the original scheme, the modified VSG eliminates the noticeable delay of the GFL's converter.

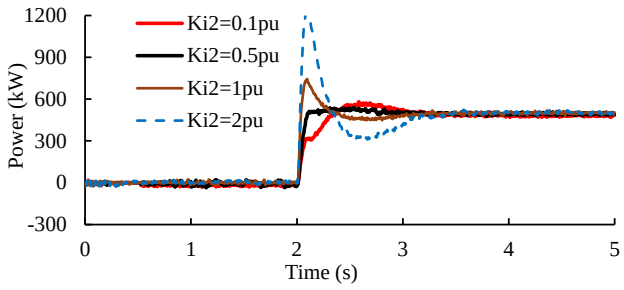

(a)

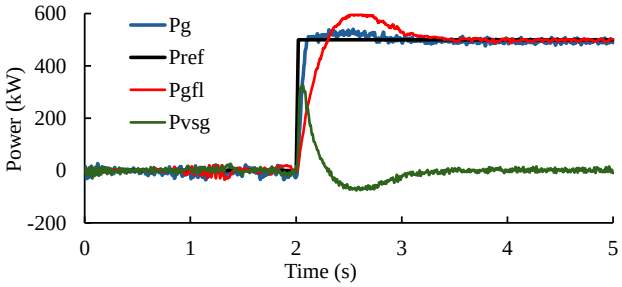

(b)

Fig.12. Power responses of tuning K_{i2} (a) different K_{i2}, (b) detailed power with $K_{i2} = 0.5pu$

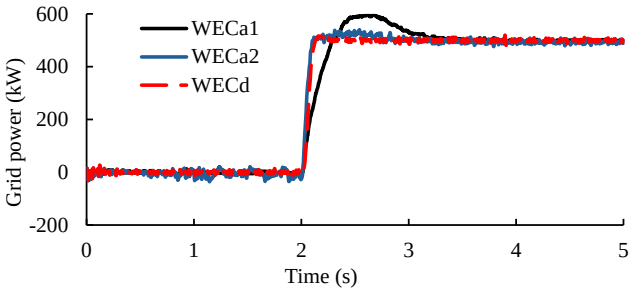

Fig. 13. Comparison between original WECa, modified WECa and WECd systems

IV. Case Study and Discussion

As mentioned in section A of II, the data acquired from PMLGs has four groups due to the symmetry of the TALOS. From the experiment, the time-series-based wave height and wavelength are obtained. Since the force from TALOS is directly proportional to the square of the wave height and inversely proportional to wavelength, the forces are calculated and shown in Fig. 14 (a). This offers a simplified theoretical basis for understanding the interaction between waves and WEC. Fig. 14 (b) shows the corresponding PMLG output power with the input of force in simulation. Fig. 15 is the simulation result which shows the effectiveness of the proposed modified WECa system. The original WECa cannot accurately follow all the power output of PMLGs, but the modified VSG can improve the WECa with more accuracy in tracking MPPT or forecasted power.

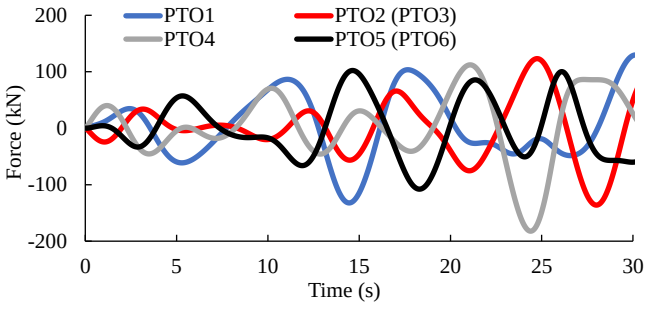

(a)

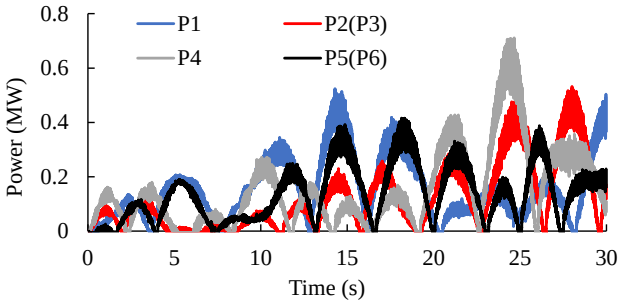

(b)

Fig. 14. Experimental data. (a) forces from TALOS, (b) power of six PMLGs

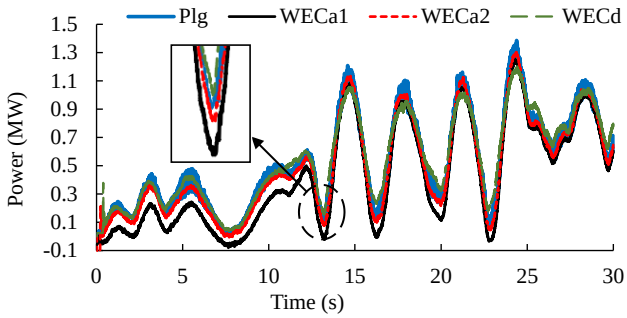

Fig. 15. Comparison between all three systems

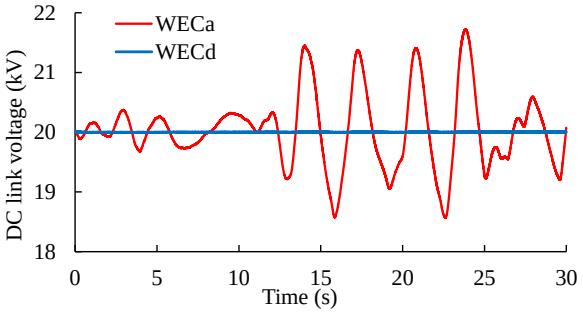

(a)

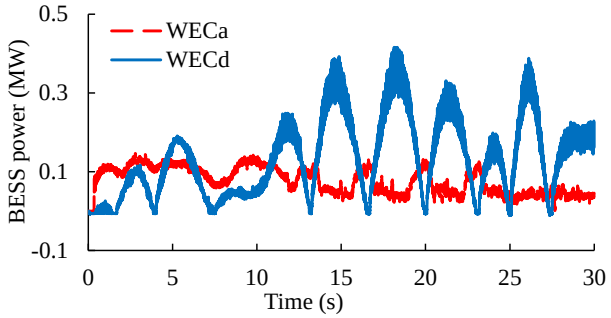

(b)

Fig. 16. Modified WECa and WECd (a) DC link voltage, (b) power of BESS

Fig. 16 (a) shows the comparison between modified WECa and WECd system. It can be observed that the significant variations of the DC link voltage of the WECa system, which is caused by the continuously changing wave power. Fig. 16 (b) shows the power output of BESS.

The significant difference indicates that when placing BESS at the DC link, the battery power has significant fluctuation due to the purpose of voltage regulation, while BESS on the AC side has lower peak power requirement.

V. CONCLUSION

This paper investigates PMLG based WEC power conversion systems with BESS at different locations. In the WECa system, where BESS is connected to the AC grid, the VSC does not require capacity expansion. However, if the BESS in the WECa system uses traditional VSG control, it results in output power delays and inaccurate power tracking. To address this problem, this paper proposes a modified VSG that improves the WECa system's performance and reduces battery peak power requirement. The development and analysis of transfer functions facilitate parameter tuning, demonstrating that the modified VSG has the same damping ratio and natural frequency as a traditional VSG, and K_{i2}&K_{p2} can be tuned to obtain desired outputs. The case studies validate the effectiveness of the modified VSG in power tracking and demonstrate that it reduces the peak power requirement of BESS. This suggests that a smaller battery could match the performance of the WECd system. As for future work, while the VSG control in this paper focuses only on the active power control loop for simplification, subsequent investigations will expand to include reactive power regulation in various scenarios. Coordination control about energy management system with the consideration of the state of charge (SoC) and wave profiles will be researched as well.

REFERENCES

[1] "Renewable energy targets", European Commission, 2023, online: https://energy.ec.europa.eu/topics/renewable-energy/renewable-energy-directive-targets-and-rules/renewable-energy-targets_en

[2] C. Hall, W. Sheng, Y. Wu, G. Aggidis, "The impact of model predictive control structures and constraints on a wave energy converter with hydraulic power take off system" in *Renewable Energy*, vol. 224, 2024.

[3] G.A. Aggidis, C.J. Taylor, "Overview of wave energy converter devices and the development of a new multi-axis laboratory prototype", IFAC-PapersOnLine, vol. 50, 2017, pp. 15651-15656.

[4] R. Guo, Y. Wu, X. Ma, G. Aggidis and N. Zhao, "Grid Integration of a Novel Linear-Generator-Based Wave Power Conversion System," *2024 International Conference on Smart Energy Systems and Technologies (SEST)*, Torino, Italy, 2024, pp. 1-6.

[5] Jusoh, M.A.; Ibrahim, M.Z.; Daud, M.Z.; Albani, A.; Mohd Yusop, Z. "Hydraulic Power Take-Off Concepts for Wave Energy Conversion System: A Review", in *Energies*, 2019.

[6] I. López, J. Andreu, S. Ceballos, I. M. de Alegría, I. Kortabarria, "Review of wave energy technologies and the necessary power-equipment", in *Renewable and Sustainable Energy Reviews*, vol. 27, pp. 413-434, 2013.

[7] Faiz, J. and Nematsaberi, A. "Linear electrical generator topologies for direct-drive marine wave energy conversion- an overview". *IET Renewable Power Generation*, pp. 1163-1176, 2017

[8] R. Datta and V. T. Ranganathan, "Variable-speed wind power generation using doubly fed wound rotor induction machine-a comparison with alternative schemes," in *IEEE Transactions on Energy Conversion*, vol. 17, no. 3, pp. 414-421, Sept. 2002.

[9] EirGrid Group. "EirGrid Grid Code", 2021, version 10, [Online] Available:https://www.eirgridgroup.com/site-files/library/EirGrid/GridCodeVersion10.pdf

[10] A.J. Hillis, C. Whitlam, A. Brask, J. Chapman, A.R. Plummer, "Active control for multi-degree-of-freedom wave energy converters with load limiting", in *Renewable Energy*, vol. 159, pp. 1177-1187,2020.

[11] M. Jama, A. Wahyudie and S. Mekhilef, "Wave Excitation Force Estimation Using an Electrical-Based Extended Kalman Filter for Point Absorber Wave Energy Converters," in *IEEE Access*, vol. 8, pp. 49823-49836, 2020.

[12] F. Wu, X. P. Zhang, P. Ju and M. J. H. Sterling, "Optimal Control for AWS-Based Wave Energy Conversion System," in *IEEE Transactions on Power Systems*, vol. 24, no. 4, pp. 1747-1755, Nov. 2009.

[13] G. Rajapakse, S. Jayasinghe, A.Fleming, M. Negnevitsky, "Grid Integration and Power Smoothing of an Oscillating Water Column Wave Energy Converter". in *Energies*, 2018.

[14] S. Rasool, K. M. Muttaqi and D. Sutanto, "A Multi-Filter Based Dynamic Power Sharing Control for a Hybrid Energy Storage System Integrated to a Wave Energy Converter for Output Power Smoothing," in *IEEE Transactions on Sustainable Energy*, vol. 13, no. 3, pp. 1693-1706, July 2022.

[15] Ullah, M.I., Döhler, J.S., de Albuquerque, V.M., Forslund, J., Boström, C., and Temiz, I. "Multi-mode converter control for linear generator-based wave energy system". *IET Renew. Power Gener*. 1–15, 2024.

[16] Q. Gao, N. Ertugrul, B. Ding, M. Negnevitsky and W. L. Soong, "Analysis of Wave Energy Conversion for Optimal Generator Sizing and Hybrid System Integration," in *IEEE Transactions on Sustainable Energy*, vol. 15, no. 1, pp. 609-620, Jan. 2024.

[17] B. Rojas-Delgado, M. Alonso, H. Amaris, and J. de Santiago, "Wave power output smoothing through the use of a high-speed kinetic buffer," *Energies*, vol. 12, no. 11, 2019.

[18] M. Talaat, Bishoy E. Sedhom, and A.Y. Hatata, "A new approach for integrating wave energy to the grid by an efficient control system for maximum power based on different optimization techniques", *Int. Journal of Electrical Power & Energy Systems*, vol. 128, 2021.

[19] A. Mohammad-Alikhani, A. Mahmoudi, R. Khezri and S. Kahourzade, "Multiobjective Optimization of System Configuration and Component Capacity in an AC Minigrid Hybrid Power System," in *IEEE Transactions on Industry Applications*, vol. 58, no. 3, pp. 4158-4170, May-June 2022.

[20] Xin Wen, Dhaker Abbes, Bruno Francois, Modeling of photovoltaic power uncertainties for impact analysis on generation scheduling and cost of an urban micro grid, Mathematics and Computers in Simulation, Volume 183,2021, Pages 116-128.

[21] M. Trapanese, V. Boscaino, G. Cipriani, D. Curto, V. D. Dio and V. Franzitta, "A Permanent Magnet Linear Generator for the Enhancement of the Reliability of a Wave Energy Conversion System," in *IEEE Transactions on Industrial Electronics*, vol. 66, no. 6, pp. 4934-4944, June 2019.

[22] H. -P. Beck and R. Hesse, "Virtual synchronous machine," *2007 9th International Conference on Electrical Power Quality and Utilisation*, Barcelona, Spain, 2007, pp. 1-6.

[23] S. D'Arco, J. A. Suul, O. B. Fosso, "A Virtual Synchronous Machine implementation for distributed control of power converters in SmartGrids", *Electric Power Systems Research*, vol.122, pp. 180-197, 2015.

[24] Y. Li, Z. Xu and K. P. Wong, "Advanced Control Strategies of PMSG-Based Wind Turbines for System Inertia Support," in *IEEE Transactions on Power Systems*, vol. 32, no. 4, pp. 3027-3037, July 2017.

[25] Zhu Y, Liu S, Wang W. Comprehensive coordinated control strategy of PMSG-based wind turbine for system inertia support. *IET Renew. Power Gener*. 2021; 15: 1915–1926.

[26] J. Chen and T. O'Donnell, "Parameter Constraints for Virtual Synchronous Generator Considering Stability," in *IEEE Transactions on Power Systems*, vol. 34, no. 3, pp. 2479-2481, May 2019

[27] A. Yazdani and R. Iravani, Voltage-Sourced Converters in Power System, New York, NY, USA: Wiley-IEEE Press, Mar. 2010.

[28] H. Wu et al., "Small-Signal Modeling and Parameters Design for Virtual Synchronous Generators," in *IEEE Transactions on Industrial Electronics*, vol. 63, no. 7, pp. 4292-4303, July 2016.